

Do the sources of the 511 keV excess explain the anomalous CMZ ionization?

Pedro De la Torre Luque^{1,2*} Francesca Calore,^{3 †}

¹*Departamento de Física Teórica, M-15, Universidad Autónoma de Madrid, E-28049 Madrid, Spain*

²*Instituto de Física Teórica UAM-CSIC, Universidad Autónoma de Madrid, C/ Nicolás Cabrera, 13-15, 28049 Madrid, Spain*

³*Another Department, Different Institution, Street Address, City Postal Code, Country*

Accepted XXX. Received YYY; in original form ZZZ

ABSTRACT

The anomalous rate of molecules ionization observed at the Central Molecular zone (CMZ) challenges known mechanisms of ionization observed in molecular clouds across the Galaxy, due to the exceptionally high levels of ionization measured (orders of magnitude above what cosmic rays can explain) and its uniform spatial distribution within the CMZ. Recent studies suggest that the source of the 511 keV excess can be correlated with this anomalous ionization rate or contribute significantly to the ionization in the Galactic Centre (GC). One of the leading hypotheses attributes the 511 keV signal to positron injection from radionuclides or pulsars distributed following the stellar bulge, which is rather flat around the GC and, hence, could help explaining the uniform ionization profile. In this work, we investigate whether such a population of sources, injecting MeV positrons at rates consistent with the 511 keV observations, can account for the ionization levels and distribution observed in the CMZ. Our results indicate that positron injection alone falls short at explaining the anomaly, although their expected ionization is larger than expected from any previously studied candidates.

Key words: Cosmic rays – β^+ radionuclides – 511 keV line – MeV gamma rays – ISM ionization

1 INTRODUCTION

Observations of the 511 keV line emission have been long pursued to study sources of positrons in the Galaxy (III et al. 1972; Haymes et al. 1975; Leventhal et al. 1978; Siebert 2023; Prantzos et al. 2011). Positrons injected in the Galaxy interact with the interstellar medium (ISM) and lose energy through different mechanisms, until they either leave the Galaxy (the most energetic ones) or become thermal (Gues-soum et al. 2005; Guessoum et al. 1991). Once they thermalize, they have a high chance of encountering with ISM electrons (free electrons, electrons bounded to molecules or atoms or electrons in dust particles) and will either annihilate directly or form a positronium bound state (Stecker 1969; Guessoum et al. 2005). The latter process is more efficient and, especially, the cross section of charge exchange ($e^- + H_2 \rightarrow ps + H_2^-$) is more than 10^6 times larger than the Dirac e^+e^- direct annihilation cross sections (Jean, P. et al. 2009). Therefore, it is expected that the 511 keV emission is related not only to the positrons injected but also to the medium where they become thermal and its gas distribution.

After decades of observations, we still do not understand the very high intensity of 511 keV photons observed around the center of the Galaxy - the so-called “positron puzzle”, which requires the injection of a large flux of positrons, at an estimated rate around a few times $10^{43} e^+/s$ (Siebert et al. 2016a; Aharonian & Atoyan 1981; Kierans et al. 2019). Different sources have been proposed to explain the

morphology and intensity of the signal. We list below some of the most popular candidates (Prantzos et al. 2011):

- The radioactive decay of β^+ unstable isotopes formed in different systems is a guaranteed source of positrons in the Galaxy (Clayton 1973; Aharonian & Atoyan 1981; Chan & Lingenfelter 1993). Since massive stars should be more concentrated around the Galactic center (GC), these sources received special attention as potential explanation of the 511 keV excess (Diehl et al. 1995; Knödlseder et al. 2005; Weidenspointner et al. 2006; Siebert 2023). In particular, the production of ^{26}Al from massive stars is expected to be an important fraction (between 10% and 100%) of the 511 keV photons observed in the Galactic disk (Prantzos et al. 2011; Skinner et al. 2015; Siebert et al. 2022). On top of that, another guaranteed contribution must come from radionuclides produced in supernovae (SNe) (as ^{44}Ti in core-collapse SNe or ^{56}Co – produced in type IA SNe), or ^{22}Na .

- Accreting binary systems are also expected to produce positrons and accelerate them (Paredes 2005; Li & Liang 1996; Guessoum et al. 2006; Bandyopadhyay et al. 2009). Microquasars have long been proposed as a source of Galactic positrons – from the potential detection of 511 keV photons from the “Great Annihilator” by SIGMA (Mirabel et al. 1992) (but later refuted by Smith et al. (1996)). However, Guessoum et al. (2006) constrained their contribution to be lower than $\sim 3 \cdot 10^{41} e^+ s^{-1}$ under the assumption that they are steady positron emitters. While high-mass X-ray binaries are found correlated with young stars and primarily distributed across the disk, low-mass X-ray binaries (LMXB) are strongly concentrated towards the Galactic bulge, and are promising source candidates.

* E-mail: pedro.delatorre@uam.es

† E-mail: francesca.calore@lapth.fr

These sources are expected to release positrons with a spectrum that roughly follows a power law.

- Other compact objects like pulsars are also candidates to inject positrons in the interstellar medium. The PAMELA positron excess (Adriani et al. 2009) and, then, the discovery of TeV-halos (Abeysekara et al. 2017) supports predictions foreseeing these sources as high-energy positron emitters (Hooper et al. 2009; Yüksel et al. 2009). In particular, millisecond pulsars are an interesting candidate for the 511 keV excess, and are still among the most promising explanation of the *Fermi*-LAT GC Excess (Murgia 2020). They are expected to follow the bulge distribution and inject positrons following power-law trends.

- A more exotic possibility is the one of sub-GeV dark matter annihilation (Boehm et al. 2004b). Dark matter is expected to be concentrated in the inner Galaxy, following an Navarro-Frenk-White distribution (Navarro et al. 1996, 2004) or something even more contracted¹. The spatial distribution of the 511 keV excess is tantalizingly similar to the expected dark matter distribution in the Milky Way from the Navarro-Frenk-White N-body simulations (Boehm et al. 2004a; Ascibar et al. 2006; De la Torre Luque et al. 2024). Interestingly, Muru et al. (2025) has recently shown that the dark matter distribution can be affected by the presence of baryons in Milky Way-like Galaxies, deforming the dark matter distribution to be similar to that of the bulge. From a particle physics perspective, candidates are tightly constrained by cosmology and may require fine-tuning, though viable options consistent with current limits still exist (Boehm et al. 2004a; Capiello et al. 2023; Aghaie et al. 2025; Balaji et al. 2025).

- Accretion around the supermassive black hole at the GC (Sgr A*) can produce non-thermal emissions, including positrons (Totani 2006). This source has been also invoked, and there have been several attempts to find a signal in INTEGRAL data (Knödlseeder et al. 2005; Jean et al. 2005; Siegert et al. 2016b). However, the current limitations (mainly the poor spatial resolution of INTEGRAL) make it difficult to identify such a component.

All of these sources may potentially provide large positron injection rates; however, quantitative estimates are highly uncertain, and direct measurements of their positron injection are not accessible with current experimental capabilities. Nevertheless, their spatial distributions may offer a way to constrain their relative importance. In this regard, a template fit analysis of the 511 keV line (Siegert et al. 2022) found that the signal favors a bulge distribution over other templates, when analyzing the signal along with the continuum ortho-positronium contribution. On top of this, the same analysis found evidence for positrons injected with low energies $E_{e^+} \lesssim 1.5$ MeV, giving further support to the radionuclides hypothesis. Such a low energy positron injection spatially associated to the 511 keV excess has recently found further evidence from an analysis of COMPTEL data Knödlseeder et al. (2025), where the authors found a significant in-flight positron annihilation signal that is well explained with positron injection at ~ 2 MeV (total energy). In sum, although systematic uncertainties in these analyses are still sizable, the latest analyses suggest the injection of low energy (\sim MeV) positrons roughly following the bulge distribution as responsible for the 511 keV line GC signal.

Another anomaly has recently been related with the injection of MeV particles around the GC: An unexpectedly high ionization rate of gas around the GC, particularly in the Central Molecular Zone

(CMZ). The CMZ is a dense molecular gas region that extends over ~ 200 pc in radius and ~ 100 pc high around the GC, with an average gas density of about $n_{\text{H}_2} \sim 150 \text{ cm}^{-3}$. Different astrochemical tracers, and especially rovibrational lines of H_3^+ transitions, have revealed an unexpectedly high ionization rate of molecular hydrogen in this region, that can be as high as $\zeta \sim 10^{-14} - 10^{-15} \text{ s}^{-1}$ (Oka et al. 2005; Oka & Geballe 2020; Geballe & Oka 2010; Indriolo et al. 2009; Le Petit et al. 2016; Coutens et al. 2017; Indriolo et al. 2015; van der Tak et al. 2006). This value exceeds the ionization rates measured in dense clouds ($\zeta \sim 10^{-17} \text{ s}^{-1}$) by two to three orders of magnitude (Indriolo et al. 2015; Phan et al. 2018), and surpasses the predicted ionization rates from cosmic rays by at least two orders of magnitude (Ravikularaman et al. 2025). This may indicate the presence of a source population (or a very diffuse/extended source) highly concentrated around the GC that is emitting ionizing particles that lose their energy very quickly, via ionization of molecular gas (Indriolo et al. 2009). The roughly uniform values of ζ measured throughout the CMZ make the anomaly even more striking, given that the main ionization candidates (particle emissions from SgrA*, point-like sources of high-energy emissions and diffuse cosmic rays) lead to strong radial dependence of the produced ionization (Dogiel et al. 2014; Ravikularaman et al. 2025). We also note that a recent study from Obolentseva et al. (2024) argued that ionization rates measured in different dense molecular clouds were biased towards higher values, due to incorrect assumptions on their line-of-sight sizes and densities. However, this correction cannot explain the anomalously large ionization observed in the CMZ, whose geometry and gas properties are comparatively well measured, although it may partially lower the inferred CMZ ionization level.

Signal correlations can be extremely useful to understand the origin of this long standing excesses. In this work, we plan to test whether the emission of positrons explaining the 511 keV signal implies a very large rate of ionization of hydrogen in the CMZ - as the one that is observed - if these positrons are produced by sources following the bulge distribution in our Galaxy. While the impact onto the 511 keV signal from different gas phases has been studied in several works, the effects of the correlated positron injection on the gas surrounding the GC have never been explored. Discussing this, and in particular, estimating the ionization produced in the CMZ by the positron sources that can potentially explain the 511 keV excess is the scope of this paper. To do this, we adopt different assumptions on the distribution of these sources, following the bulge structure, and the spectral dependence of the positron injection. Finally, we discuss how relevant is such an injection of particles concentrated around the CMZ for the star formation rate and the dynamics of particle diffusion within such a structure.

This paper is structured as it follows: We first describe the bulge distribution that we use to evaluate the positron source distribution in Sect. 2.1. Then we discuss the positron injection spectrum and how this is normalized to the observed positron injection rate in sections 2.2 and 2.3, respectively. Then, we report the expected ionization rates and their spatial profiles in the CMZ for the different cases studied, in Section 3. Our conclusions are summarized in Sect. 4.

2 METHODOLOGY

2.1 Bulge distributions

In our estimations, we employ the state-of-the-art parameterizations of the observed Galactic bulge distribution, combining a nuclear

¹ Note that current observations of the Milky Way do not allow us to robustly constrain the dark matter density in the inner Galaxy – e.g. Gardner et al. (2021)

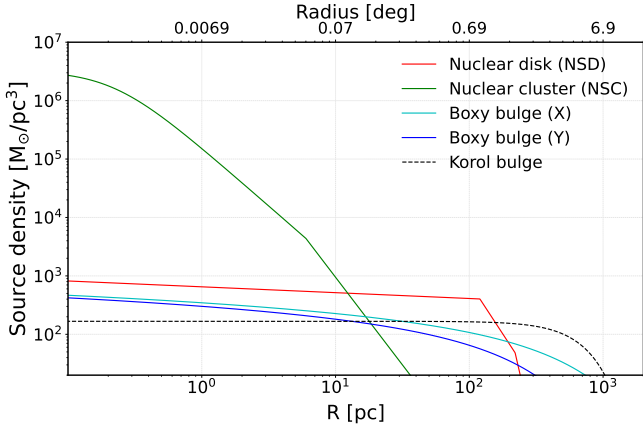


Figure 1. Comparison of the different components and models for the source distribution in the Galactic bulge, described in the text. The figure illustrates the source density as a function of radial distance from the center of the Galaxy, with the normalizations detailed in the main text.

bulge, with a larger-scale bulge. For the latter, we use two representative cases described below.

Korol distribution: As a representative case for the bulge distribution we employ the parameterization given in Korol et al. (2018), which features a radially symmetric bulge with an exponential decrease in density of stars, following:

$$\rho = \rho_0 \cdot \exp\left(-\frac{r^2}{2r_b^2} - \frac{z}{z_b}\right), \quad (1)$$

where r is the radial distance from the GC in the plane of the Galaxy and z represents the vertical coordinate. r_b and z_b are set to 500 and 200 pc, respectively. As we describe later (Sec 2.3), the normalization density is set by imposing that the total injection rate of positrons is the one inferred from the 511 keV observations.

Boxy-Bulge distribution: The second model for the boxy-bulge follows the parameterizations fit by the triaxial E3 model explored in Cao et al. (2013); Dwek et al. (1995), which tracks the distribution of Red Clump Giant stars (Nataf et al. 2013) that is obtained from surveys like OGLE/VVV (Minniti et al. 2010):

$$\rho_{\text{BB}} = \rho_0 \cdot K_0(r_{\text{BB}}) \quad (2)$$

where $K_0(r_{\text{BB}})$ is the Bessel function of second kind and order 0, and

$$r_{\text{BB}} = \left(\left[\left(\frac{x}{x_0} \right)^2 + \left(\frac{y}{y_0} \right)^2 \right]^2 + \left(\frac{z}{z_0} \right)^4 \right)^{1/4},$$

where $x_0 = 67$ pc, $y_0 = 29$ pc, and $z_0 = 27$ pc. This distribution is the most popular one for studies related to the Galactic center excess, and was found to agree well with the 511 keV signal distribution (Siebert et al. 2022).

For the nuclear bulge, we consider two components:

Nuclear stellar disk (NSD):

$$\rho_{\text{NSD}}(r) = \begin{cases} \rho_0 \left(\frac{r}{1 \text{ pc}} \right)^{-0.1} \cdot e^{-\left(\frac{|z|}{45 \text{ pc}} \right)} & r < 120 \text{ pc} \\ \rho_1 \left(\frac{r}{1 \text{ pc}} \right)^{-3.5} \cdot e^{-\left(\frac{|z|}{45 \text{ pc}} \right)} & 120 \text{ pc} < r < 220 \text{ pc} \\ \rho_2 \left(\frac{r}{1 \text{ pc}} \right)^{-10} \cdot e^{-\left(\frac{|z|}{45 \text{ pc}} \right)} & r > 220 \text{ pc}, \end{cases} \quad (3)$$

where r stands for the distance from the center at a given height (z

coordinate) (i.e. $r = \sqrt{x^2 + y^2}$). The normalizations at different r are set such as the function is continuous at the breaks (Launhardt et al. 2002).

Nuclear stellar cluster (NSC):

$$\rho_{\text{NSC}}(r) = \begin{cases} \rho_0 \left(1 + \left(\frac{r}{r_0} \right)^2 \right)^{-1} & r < 6 \text{ pc} \\ \rho_1 \left(1 + \left(\frac{r}{r_0} \right)^3 \right)^{-1} & 6 \text{ pc} < r < 200 \text{ pc} \\ 0, & r > 200 \text{ pc} \end{cases} \quad (4)$$

where the normalizations at different r are set such as the function is continuous at the breaks. Here, r represents the spherically symmetric distance from the center of the Galaxy ($r = \sqrt{x^2 + y^2 + z^2}$) and $r_0 = 0.22$ pc (Portail et al. 2015).

In what follows, we will either use these bulge components separately or combine the boxy-bulge distribution with the nuclear bulge. The latter combination is indeed a more complete description of the source distribution at the bulge. In this case, even though we still normalize the total positron injection rate to the one corresponding to the 511 keV observations as we will explain below, the relative normalization of each component will be fixed by the stellar distributions. To do so, we follow Bartels et al. (2018) and set the normalizations of the different components to be: For the boxy-bulge, $\rho_0^{\text{BB}} = 52.1 \text{ M}_\odot \text{ pc}^{-3}$ is set such as the total bulge mass is $9.1 \cdot 10^9 \text{ M}_\odot$ (Licquia & Newman 2015). $\rho_0^{\text{NSD}} = 301 \text{ M}_\odot \text{ pc}^{-3}$ to get a total mass enclosed in the inner 120 pc of $8 \cdot 10^8 \text{ M}_\odot$ (Launhardt et al. 2002). $\rho_0^{\text{NSC}} = 3.27 \times 10^6 \text{ M}_\odot/\text{pc}^3$, such that the total mass enclosed in the inner 625 pc is $7 \cdot 10^5 \text{ M}_\odot$ (Launhardt et al. 2002).

In Figure 1, we show a comparison of the different distributions discussed above in logarithmic scale to show the innermost region around the GC. The normalization of each component is the one commented above. In this panel, we indicate with two different lines the density trend with distance from the GC in the two perpendicular directions at the Galactic plane (X and Y, in the labels), given that the boxy-bulge template is non radially symmetrical. A similar figure, but including also a Navarro-Frenk-White-like dark matter density distribution is shown in Appendix A, Figure A1.

2.2 Positron injection spectra

As discussed above, the injection of positrons from different sources might have different spectral trends with energy, from line-like injections to power-law trends. We here consider three different spectral behaviors: a first, phenomenological one, a second one corresponding to more realistic radionuclides spectra, and a third one representing pulsar-like spectra.

Log-normal spectrum. We first test a general case where the positron injection is modeled following a log-normal spectrum (upper panel of Fig. 2). This has the advantage to be flexible enough to capture the behavior expected from injection of radionuclides (see lower panel of Fig. 2) and also line-like injection features like the ones expected from dark matter. The main parameter (mostly affecting the ionization phenomenology) is here the mean energy of the injected positrons. We parameterize this log-normal injection as:

$$\frac{dN_{e^+}}{dE} \propto \frac{1}{E \sigma_E \sqrt{2\pi}} \exp\left[-\left(\frac{\ln(E) - \ln(E_{\text{mean}})}{2\sigma_E}\right)^2\right], \quad (5)$$

σ_E is given by imposing the width of the spectrum to be a fraction of the mean energy, i.e. standard deviation is $E_{\text{mean}} \times f$, where f is the fraction of the mean energy that sets how wide is the signal.

From this, σ_E is defined as $\sigma_E = \sqrt{\ln(1 + (E_{\text{mean}} \times f)^2)}$ (Aitchison & Brown 1957; Limpert et al. 2001).

Here, we set standard deviation of the log-normal distribution to be 1/50 of the mean energy (i.e. $f = 1/50$ is used as default). We have tested that changing this value from 1/500 to 1 times the mean energy leads to changes that are not higher than $\sim 15\%$ in the total ionization rate predicted. The reason for this, is because the signal is always normalized to the total rate of positrons injected in the inner 8 deg, as we describe in Sect. 2.3. In these calculations, we have considered values of E_{mean} from 0.1 MeV to 20 MeV for the reasons that will be discussed later. In the example shown in Fig. 2, we represent, in the upper panel, the general signals (following a log-normal distribution) for different positron mean energies. For concreteness, the x -axis represents the positron kinetic energy.

β^+ -radionuclides spectrum. The spectrum of β^+ unstable isotopes produced in stars, SNe or novae, such as ^{56}Co , ^{44}Ti , ^{26}Al , or ^{22}Na , can be approximated as (Conti & Eriksson 2016; Stabin & Siegel 1979; Landstreet 2002):

$$\frac{dN_{e^+}}{dE_{e^+}} \propto \sqrt{E_{e^+}^2 + 2E_{e^+}m_e} \cdot (Q - E_{e^+})^2 \cdot (E_{e^+} + m_e) \cdot F(E_{e^+}, Z). \quad (6)$$

Note that the proportionality constant is not relevant here, since we will require the integrated spectrum to yield the required positron injections rate to explain the 511 keV signal. Q represents the energy yield of the transition and as such is the upper bound on the kinetic energy of the positron, E_{e^+} , and Z is the atomic number of the radionuclide. For the cases that we study, we use $Q_{^{26}\text{Al}} = 1.173$ MeV, $Q_{^{22}\text{Na}} = 0.5455$ MeV, $Q_{^{44}\text{Sc}} = 1.474$ MeV and $Q_{^{56}\text{Co}} = 1.46$ MeV. The Fermi function, $F(E_{e^+}, Z)$ is approximately given by (Landstreet 2002)

$$F(E_{e^+}, Z) \simeq \frac{2\pi\eta}{1 - \exp(-2\pi\eta)}, \quad (7)$$

with $\eta = -Z\alpha_c/c\beta_e$, where, α_c is the fine structure constant and $c\beta_e$ is the positron speed in speed of light units. We show the spectra for each of these nuclei in the bottom-left of Fig. 2 in arbitrary units, and also in Fig. A2 but with the normalization of the injection spectrum that leads to the adopted positron rate within the bulge. Compared with the phenomenological spectrum, these injections are similar to the log-normal parametrization for positrons with kinetic energy ~ 1 MeV and a large σ_E value (leading to broader signals).

Pulsar spectrum. Finally, we explore the case of injection of low energy electrons and positrons injected following power-law spectra, as expected from pulsars or X-ray binaries (Guessoum et al. 2006; Bandyopadhyay et al. 2009). Since we normalize our spectrum to the total injected positron rate (see below), the power-law requires setting a minimum positron energy (otherwise all electrons and positrons are injected at kinetic energies below the minimum ionization energy, that is about 15 eV). Therefore, we parametrize this injection as

$$\frac{dN_{e^+}}{dE_{e^+}} \propto \left(\frac{E}{E_0}\right)^{-\gamma} \exp(-E/E_{\text{cut}}), \quad (8)$$

where E_0 is set to 0.1 MeV and varied to see its impact. We show this injection in the lower-left panel of Fig. A2, where the legend represents different values of the cutoff energy and we use $\gamma = 2.2$ there.

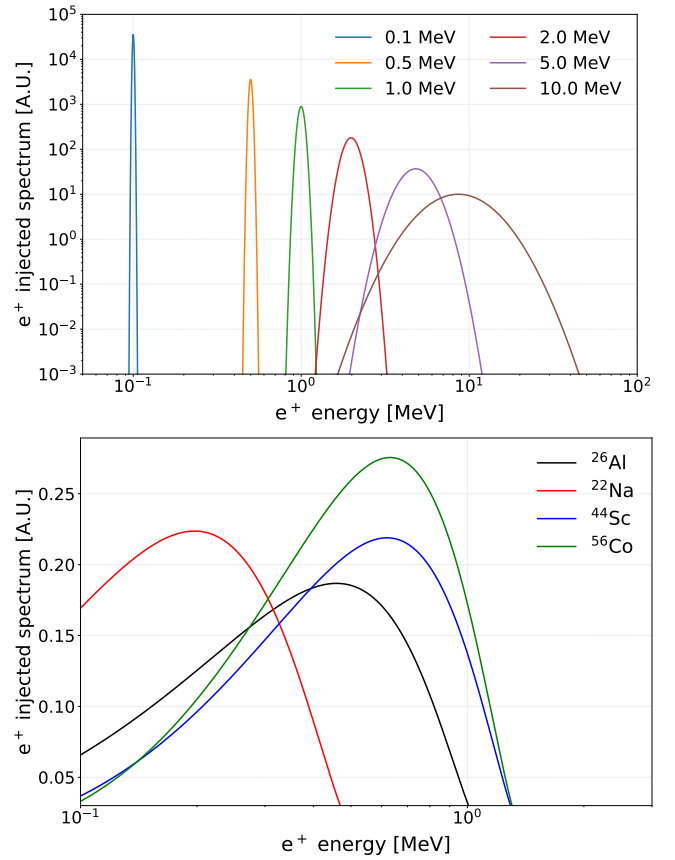


Figure 2. Top panel: Positron injection spectra of the signals described by Eq. 5 for different mean energies (indicated by the colors in the legend). The width of each spectrum is fixed to one-fiftieth of its mean energy. **Bottom panel:** Injection spectra for different β^+ radionuclides commonly associated to massive stars, SNe and novae, as indicated in the legend.

2.3 511 keV line signal normalization

After injection, positrons interact with the gas and propagate, eventually becoming thermal and finding ambient electrons with which they interact and produce 511 keV photons. Given the low energy of these positrons the dominant time-scale for these positrons is that of energy losses from ionization of the gas, such that diffusion can be neglected (see e.g. Fig. 3 in the Appendix of De la Torre Luque et al. (2025) for the comparison between different time scales in the GC). We note that this approximation is valid for low energy particles – below a few tens of MeV – and in dense media, and it has the advantage that it does not need to assume a diffusion coefficient or other propagation parameters that are not known at all near the GC. Including diffusion and/or advection would slightly flatten the positron spatial distribution compared to what is shown in Fig. 1. Under this assumption, the steady-state distribution of positrons can be calculated as

$$\frac{dn_{e^+}}{dE}(E, \mathbf{x}) = \frac{1}{b_e(E, n_{H_2})} \int Q_e(E', \mathbf{x}) dE', \quad (9)$$

with b_e as the energy-loss term from ionization ($b_e \equiv (dE/dt)_{\text{ion}}$), calculated following the one implemented in the DRAGON2 code (see Eq. (C.39) of Evoli et al. (2017)), $n_{H_2}^{\text{CMZ}} = 150 \text{ cm}^{-3}$ is taken as the mean density of the CMZ (Ravikularaman et al. 2025; Indriolo et al. 2015), using a mixture of H and He of 1/10, and $Q_e(E_e, \mathbf{x}) = Q_0$.

$\rho_{\text{Bulge}}(x, y, z) \cdot \frac{dN}{dE_e}(E_e)$ is the source term (injection spectrum). Here, the normalization, Q_0 is described in the next section, $\frac{dN}{dE_e}(E_e)$ is the positron injection and ρ_{Bulge} is the density distribution described above (which comes from the sum of the different components). Note that this source term follows the distribution of sources in the bulge and, thus, it makes the spatial distribution of positrons to follow the bulge density distribution.

Variations in the gas density distribution could lead to variations in the distribution of electrons and positrons and, hence, in the ionization rate profile. Our estimations assume a spatially uniform gas density throughout the CMZ, which is a reasonable approximation on scales beyond the circumnuclear disk (i.e. above 1-5 pc). Nevertheless, observations reveal a marked longitudinal asymmetry, characterized by higher densities at positive longitudes, although no clear global trend in the gas density is evident. In turn, latitudinal asymmetries are relatively mild (Battersby et al. 2025). Moreover, dense clumps and cores are present throughout this region, their volume filling factor is small and they do not significantly affect this assumption.

In order to link the expected CMZ ionization rate with the 511 keV observations, we normalize the positron spectra obtained by imposing the rate of positrons required to explain the 511 keV observations of the bulge. Therefore, we impose that the positron injection rate from these sources² is $2 \cdot 10^{43} \text{ e}^+/\text{s}$ in the inner 8 deg (Siebert et al. 2016b; Skinner et al. 2015). Specifically, we impose this positron injection rate within the volume enclosed in the inner 1.15 kpc of the GC, which corresponds to an angular radius of 8 deg in the inner Galaxy. Said in other words, Q_0 is obtained by integrating the positron flux over energy and over the inner 8 deg (the bulge) to provide a positron rate of $2 \cdot 10^{43} \text{ e}^+/\text{s}$.

$$\int_{\text{Bulge}} dV \int dE Q(E, \mathbf{x}) = Q_0 \int_{\text{Bulge}} dV \rho_{\text{Bulge}} \int dE \frac{dN}{dE}(E, \mathbf{x}) = 2 \cdot 10^{43} \text{ e}^+/\text{s}, \quad (10)$$

This normalization ensures that the total ionization rate would not change even including propagation effect (provided that the positron rate to which we normalize is the total number of positrons in the bulge), although the ionization profile could slightly flatten, as commented above.

2.4 Ionization rate in the CMZ

Given the positron density within the CMZ, calculated from Eq. 9, the positron flux, $J(E, \mathbf{x})$, can be computed as

$$J_e(E, \mathbf{x}) = \frac{dn_{e^+}}{dE}(E, \mathbf{x}) \frac{\beta_e(E)c}{4\pi}, \quad (11)$$

where $\beta_e(E)c$ is the speed of the positron. Finally, with this flux we compute the rate of ionization of molecular hydrogen within the CMZ as (Padovani et al. 2009; Phan et al. 2023)

$$\zeta(\mathbf{x}) = 4\pi \int_{E_{\min}}^{E_{\max}} J_e(E, \mathbf{x}) \sigma(E)(1 + \theta_e(E))dE, \quad (12)$$

where E_{\max} is the maximum kinetic energy with which the positrons are injected and E_{\min} is the minimum kinetic energy to produce ionization in the gas (15.43 eV Padovani et al. (2009); Phan et al. (2023)), $\sigma(E)$ is the $e\text{-H}_2$ cross-section, calculated as in Eq. (7) of Padovani et al. (2009) and $\theta_e(E)$ is the number of secondary ionizations per primary ionization, calculated as Eq. (2.23) of Krause et al. (2015). Note that the spatial dependence of the ionization rate is inherited by the distribution of the injected electrons and positrons.

The calculations above can be applied in general for any spectral dependence of the source term.

3 RESULTS

In this section, we present our results, derived for different components of the bulge and their combination, as well as for different injection spectra based on the potential sources of the 511 keV excess discussed above.

3.1 General case: log-normal injection spectrum of positrons

Following the calculation described above, we show, first, in Fig. 3 the expected ionization rate in the inner few hundreds parsecs of the Galaxy (corresponding to the CMZ region) for the general case of log-normal injection spectrum of positrons, following the different source density distributions commented in Sect. 2.1. The different colors represent the ionization rate expected for positrons injected with the mean energy indicated in the legend in every case. The top-left panel refers to the ionization rate calculated assuming only the boxy-bulge distribution (Eq. 2), which is the dominant one at large distances at the edges of the CMZ. The resulting ionization rates are very similar to those obtained when assuming a symmetric bulge distributed of Korol et al. (2018), since the two models provide very similar descriptions of the bulge. In the upper-right panel, we display the radial profile of the ionization rate calculated using the NSD source-density distribution (Eq. 3). This distribution constitutes the main mass component within the inner 200 pc.

As we see, in both cases the predicted level of ionization rate is significantly below $\sim 10^{-15} \text{ s}^{-1}$, which is around the minimum value required to explain the abundances of ionized hydrogen (Oka et al. 2005; Oka & Geballe 2020; Geballe & Oka 2010; Indriolo et al. 2009). However, although the expected ionization rate is much lower than observed, the values of ionization rate obtained adopting the NSD distribution are significantly larger than those from the boxy-bulge case, which is due to the fact that the source density in the inner Galaxy is much larger than the density outside the CMZ for the NSD distribution. Since the total positron injection rate is normalized to the one required to reproduce the 511 keV intensity in the whole bulge (Eq. 10), this makes most of the injected positrons be accumulated in the inner ~ 200 pc. In other words, the larger the density in the inner region of the bulge over the outer region, the larger is the expected ionization rate in the CMZ.

In these panels, one can see that, for a fixed rate of injected positrons, the higher is the energy of the positrons injected, the more they can ionize the medium, in general. This is because these positrons deposit all their energy within the CMZ and they become thermal before escaping this region. As we discussed above, this is true only for low energy positrons injected, below a few tens of MeV, where the diffusion time-scale is subdominant, and it is the reason because we restrict ourselves to a maximum positron injection energy of 20 MeV. Moreover, we checked the effect of adopting different values for the variance of the log-normal distributions describing

² Given that observations support a constant flux of 511 keV photons (in time), the injection rate must match the rate of positron annihilation.

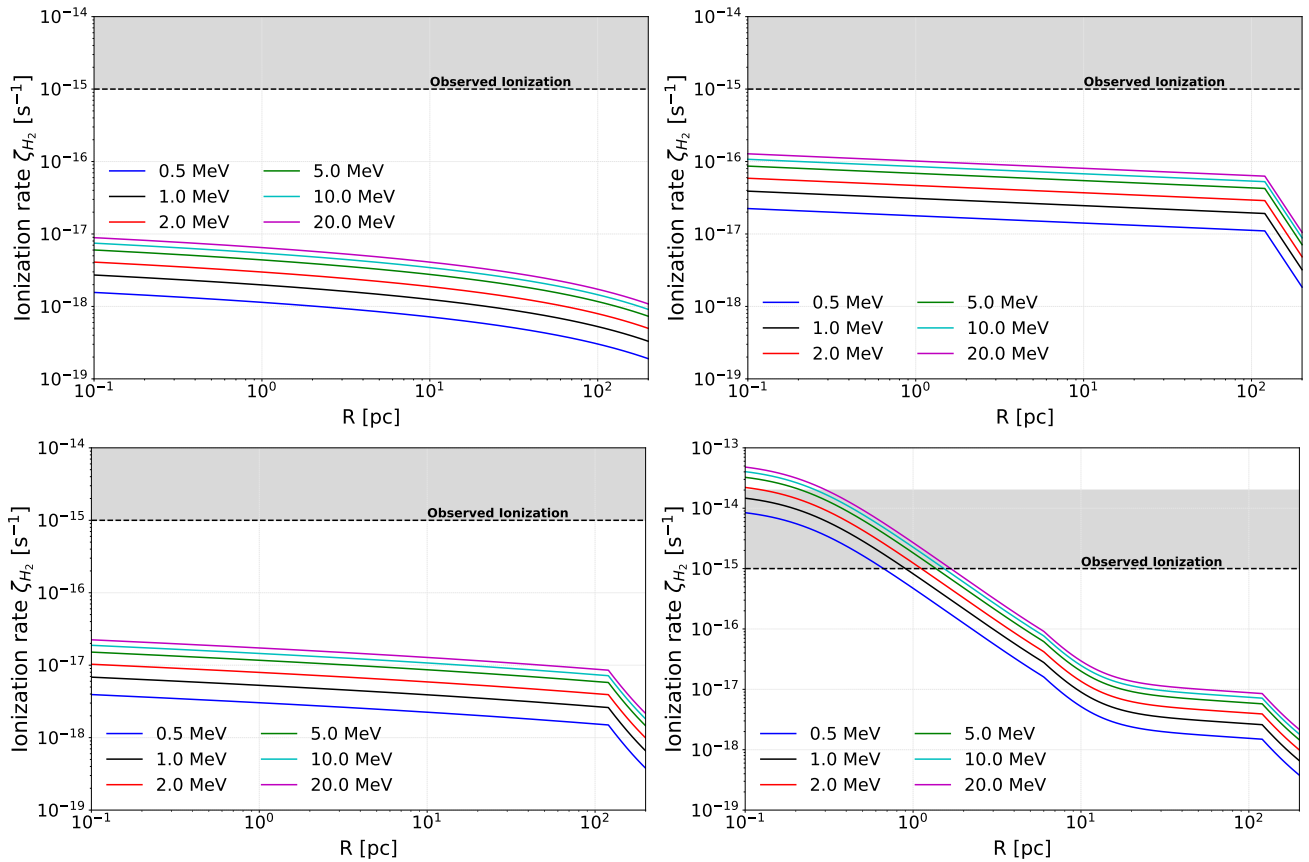


Figure 3. H_2 ionization rate expected at the CMZ from positron sources following different source density distributions and assuming an log-normal injection spectrum. **Top-left panel:** H_2 ionization rate expected from positron sources following the boxy-bulge distribution. **Top-right:** Ionization rate expected from positron sources following the nuclear stellar disk (NSD). **Bottom-left:** Expected ionization rate in the CMZ from a combination of the nuclear stellar disk and boxy-bulge distributions. **Bottom-right:** Ionization rate at the CMZ from a combination of the nuclear stellar disk, nuclear stellar cluster and the boxy-bulge distributions.

the positrons injection spectrum, and found that the ionization rate for each mean positron energy, remains very similar (with variations of the order of 15%, increasing slightly toward higher values of the variance). This is because the integrated signal is normalized to the total positron positron rate, so that making it broader or tighter does not change the total positron flux, only its spectral shape (which is why there are small variations).

Then, the bottom-left of Fig. 3 depicts the profile of the ionization rate for a combination of NSD and boxy-bulge distribution, while the bottom-right the combination of boxy-bulge with NSD and NSC distributions, which is expected to be the most realistic case. In both cases, we normalize the total injection rate after adopting the normalizations (ρ_0 values) discussed above, which sets the relative importance of each component (i.e. the total density of the summed components is not relevant but their relative contributions are very important for the signal’s morphology). As we see, the inclusion of the NSC changes significantly the expected ionization rate. Without this component, the ionization profile is expected to be very uniform in all cases, with variations of less than a factor of a few. In contrast, the inclusion of the NSC significantly boosts the ionization rate in the inner parsec, bringing it to – or even above – the observed level. However, this also causes the expected ionization profile to vary strongly with distance from the GC, changing very quickly. Although radial winds and positron diffusion would tend to flatten the profile, the expected ionization varies by 2–3 orders of magnitude

beyond the inner parsec³, making the profile too steep to match the observations. This conclusion is further supported from what we show in Sect. 3.2. A detailed study of the effects of such winds would be necessary to reach a definitive conclusion. Remarkably, we note that these values are much higher than those usually expected from cosmic rays penetrating the CMZ, or even than other sources of high-energy particles known to be in this region (Ravikularaman et al. 2025).

3.2 Specific cases for the positron injection spectrum

In this section, we adopt specific spectral distributions for the injected positrons, based on two general parametrizations of the potential 511 keV sources described above: The general spectrum of β^+ decay from radionuclides and a power-law with an exponential cutoff.

As we see from the left panel of Fig. 4, positrons from radionuclides would lead to a similar level of ionization to the one presented in the generic spectrum shown above for a mean injection energy of around 1 MeV, which is clearly insufficient to explain the ionization rate level observed in the CMZ. However, we stress that in the processes in which these radionuclides are expected to be produced,

³ the resolution for measurements of rovibrational lines of ionized molecules – in particular, in the infrared and for H_3^+ – are typically above a fraction of a parsec

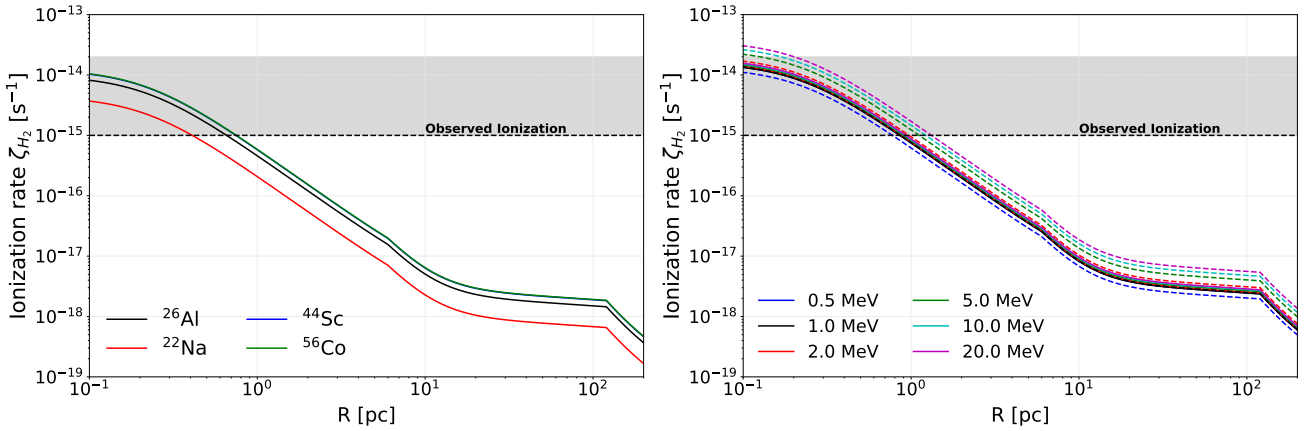


Figure 4. H_2 ionization rate expected at the CMZ from positron sources following a combination of the nuclear stellar disk, nuclear stellar cluster and the boxy-bulge distributions and assuming radionuclides injecting the positrons (left panel) and a power-law positron injection (right panel). In the left panel, the different colors indicate different radionuclides. In the right panel, the different colors indicate different cut-off energies. In this panel solid lines correspond to a power-law where the spectral index is $\gamma = 2.2$, while the dashed lines correspond to a power-law of $\gamma = 1.2$.

high-energy particles—such as protons and heavier nuclei—are generated as well. These particles should also contribute significantly to the total ionization, and they are expected to follow a similar ionization profile. Therefore, although positron injection by itself cannot explain the observed level of ionization, this does not imply that the sources producing these positrons are incapable of accounting for the measured ionization.

The expected ionization rate profile from pulsar-like injection spectra is illustrated in the right panel of Fig. 4, where different colors indicate different cutoff energies. In this case, we assume that pulsars-like sources inject same numbers of positrons and electrons, and therefore we take into account an extra factor of 2 in the calculation of the ionization rate. Here, we find that the spectral index slightly affects the predicted ionization rate (see the difference between dashed and solid lines, representing the case of $\gamma = 1.2$ and $\gamma = 2.2$, respectively). Furthermore, the impact of the cutoff energy depends on the spectral index used: A larger γ value (in absolute value) means that more positrons are distributed at the lower energies, which tends to make the estimation rate mainly driven by the value of E_0 that we use. Meanwhile, a low spectral index value (i.e. a harder spectrum) distributes more positrons at the higher energies, making the ionization rate more dependent on the cutoff energy used. Adopting a E_0 value of 1 MeV, instead of 0.1 MeV, leads to an increase of around a factor of ~ 2 . In sum, all these variations predict an ionization rate similar to the one that we see in the previous cases, where the inclusion of the NSC increases significantly the ionization level in the inner parsec, leading to a very steep profile.

As a last note here, we stress that although pulsars are likely to explain the high-energy part of the local positron flux measured by PAMELA and AMS-02 (Aguilar & others (AMS Collaboration) 2014), simulations indicate that positrons from pulsars and millisecond pulsars cannot efficiently escape and be injected into the ISM following a power-law with energies below \sim a few tens of MeV (see e.g. Timokhin (2010)), making them less suitable to explain the low energy (\sim MeV injection) required to explain the COMPTEL signal commented above. On top of this, observations of TeV halos (Abeysekara et al. 2017) support a very high-energy injection of electrons and positrons from pulsars, which would propagate long distances before thermalizing (with path-lengths to become thermal much larger than for MeV positrons (Siegert et al. 2022; la Torre Luque; Pedro et al. 2025)), making them not suitable to explain the

concentration of the 511 keV excess around the GC. Additionally, such high-energy injection would violate constraints from in-flight annihilation and diffuse emission (Sizun et al. 2006; Beacom & Yüksel 2006; Das et al. 2025). Meanwhile, X-ray binaries could inject more efficiently MeV positrons and even contribute significantly to the sub-MeV continuum diffuse emission, as shown in Kantzas & Calore (2024).

4 DISCUSSION AND CONCLUSIONS

In this paper, we investigated whether the positron injection rate required to explain the 511 keV emission observed in the Galactic bulge can also explain, or significantly contribute to, the anomalous ionization rate measured in the CMZ. To this end, we considered several spatial distributions for potential sources of the 511 keV excess, motivated by the observed stellar distribution in the Galactic bulge, and explore different parameterizations of their positron injection spectra. Given that the observed morphology of the 511 keV emission is very concentrated around the GC, and the recent hint for in-flight annihilation signal from MeV positrons detected in COMPTEL data, we focused on positrons injected below a few tens of MeV.

We found that, if the positron emission follows the boxy bulge, the NSD or the combination of these two, the total level of ionization in the CMZ remains below what is observed, with maximum values for the ionization rate that are in the range of 10^{-16} s^{-1} to 10^{-15} s^{-1} , but generally predicting a level of ionization that is around 10^{-17} s^{-1} beyond the inner pc. A notable aspect of these results is that such source distributions yield a fairly uniform spatial ionization profile within the CMZ, matching one of the most striking features observed in the CMZ ionization rate. However, including the NSC, which is highly concentrated within the \sim inner parsec, the expected ionization level increases sharply in the inner parsec, reaching ionization rates even above 10^{-14} s^{-1} , but then decreases rapidly at larger radii, falling significantly below the observed ionization level and producing a profile that is not compatible with the uniformity of CMZ measurements. This holds true either for the case of radionuclides spectra or a power-law-like positron injection, and even for line-like injections, as long as the sources injecting these positrons follow the distributions of stars in the Galactic bulge. Additionally, we note that when combining the different profiles, we assume that the positron

injection is directly proportional to the source density of each component, even though different components may host different source populations. Each of these components may hold different sources, that could change the spatial ionization profile. In this regard, the BB profile is expected to contain the older systems, while the NSC is characterized for having a higher star formation activity (Nie et al. 2026).

Our result rules out positrons from a variety of sources as the sole cause of the unexpectedly high ionization rate in the CMZ, at least within the assumption that positrons do not propagate significantly from their injection sources. However, we stress the high values of ionization expected in the inner parsec only by the positron injection that can be expected in the NSC. Including diffusion and/or advection would slightly flatten the positron spatial distribution compared to what is shown in Fig. 1. As a result, the ionization profile in the CMZ would become more uniform. Moreover, including diffuse reacceleration and advection can accelerate the injected positrons. This latter argument could reconcile the COMPTEL in-flight annihilation signal with the hypothesis of radionuclides producing the 511 keV excess. However, the total level of ionization seems insufficient to reach the ionization rate measurements in any case and the effects of including propagation with winds, diffusion and reacceleration are expected to be very minor for MeV positrons.

Most positron-producing sources, such as SNe and X-ray binaries, also emit other energetic particles that may significantly enhance the ionization and still provide a plausible explanation for this anomaly. Therefore, we still cannot exclude the possibility that the same sources producing the 511 keV excess may be the responsible of the observed levels of ionization. Accounting for the ionization induced by accelerated protons and heavier nuclei is left for a future work.

Overall, this study highlights the potential correlation between excesses associated with low-energy particle emissions in the GC. Identifying such correlations could provide a powerful means of uncovering the origin of these anomalies and constraining the properties of previously unknown sources.

ACKNOWLEDGEMENTS

The authors want to help Thomas Siebert and Sruthiranjani Ravikularaman for their useful and interesting comments and feedback. PDL has been supported by the Juan de la Cierva JDC2022-048916-I grant, funded by MCIU/AEI/10.13039/501100011033 European Union "NextGenerationEU"/PRTR, and is currently supported by Ramón y Cajal RYC2024-048445-I grant, which is funded by MCIU/AEI/10.13039/501100011033 and FSE+. The work of PDL is also supported by the grants PID2021-125331NB-I00 and CEX2020-001007-S, both funded by MCIN/AEI/10.13039/501100011033 and by "ERDF A way of making Europe". PDL also acknowledges the MultiDark Network, ref. RED2022-134411-T. This project used computing resources from the National Academic Infrastructure for Supercomputing in Sweden (NAISS) under project NAISS 2024/5-666. The work of FC is supported by the Agence Nationale de la Recherche through the project ANR-25-CE31-6485.

DATA AVAILABILITY

The data used are fully public and appropriately referenced. All our results and scripts can be shared upon request.

REFERENCES

- Abeyskara A. U., et al., 2017, *The Astrophysical Journal*, 843, 40
- Adriani O., Barbarino G. C., Bazilevskaya G. A., Bellotti R., Boezio M., Bogomolov E. A., Bonechi L., et al. 2009, *Nature*, 458, 607
- Aghaie M., De la Torre Luque P., Dondarini A., Gaggero D., Marino G., Panci P., 2025, arXiv e-prints
- Aguilar M., others (AMS Collaboration) 2014, *Physical Review Letters*, 113, 121101
- Aharonian F. A., Atoyan A. M., 1981, *Soviet Astronomy Letters*, 7, 395
- Aitchison J., Brown J. A. C., 1957, *The Lognormal Distribution*. Cambridge University Press, Cambridge, UK
- Ascasibar Y., Jean P., Boehm C., Knödseder J., 2006, *Monthly Notices of the Royal Astronomical Society*, 368, 1695–1705
- Balaji S., Cleaver D., la Torre Luque P. D., 2025, An Excited Dark Matter Solution to the MeV Galactic Center Excesses (arXiv:2512.13797), <https://arxiv.org/abs/2512.13797>
- Bandyopadhyay R. M., Silk J., Taylor J. E., Maccarone T. J., 2009, *Monthly Notices of the Royal Astronomical Society*, 392, 1115
- Bartels R., Storm E., Weniger C., Calore F., 2018, *Nature Astronomy*, 2, 819–828
- Battersby C., et al., 2025, *Astrophysical Journal*, 984, 156
- Beacom J. F., Yüksel H., 2006, *Physical Review Letters*, 97
- Boehm C., Ensslin T., Silk J., 2004a, *J. Phys. G*, 30, 279
- Boehm C., et al., 2004b, *Phys. Rev. Lett.*, 92, 101301
- Cao L., Mao S., Nataf D., Rattenbury N. J., Gould A., 2013, *Mon. Not. Roy. Astron. Soc.*, 434, 595
- Cappiello C. V., Jafs M., Vincent A. C., 2023, *Journal of Cosmology and Astroparticle Physics*, 2023, 003
- Chan K.-W., Lingenfelter R. E., 1993, *The Astrophysical Journal*, 405, 614
- Clayton D. D., 1973, *Nature Physical Science*, 244, 137
- Conti M., Eriksson L., 2016, *EJNMMI Physics*, 3
- Coutens A., Rawlings J. M. C., Viti S., Williams D. A., 2017, *Monthly Notices of the Royal Astronomical Society*, 467, 737
- Das S., Krumholz M. R., Crocker R. M., Siebert T., Eisenberger L., 2025, arXiv preprint
- De la Torre Luque P., Balaji S., Silk J., 2024, *Astrophys. J. Lett.*, 973, L6
- De la Torre Luque P., Balaji S., Silk J., 2025, *Phys. Rev. Lett.*, 134, 101001
- Diehl R., et al., 1995, *Astronomy & Astrophysics*, 298, 445
- Dogiel V., Chernyshov D., Kiselev A., Cheng K.-S., 2014, *Astroparticle Physics*, 54, 33–39
- Dwek E., et al., 1995, *The Astrophysical Journal*, 445, 716
- Evoli C., Gaggero D., Vittino A., Bernardo G. D., Mauro M. D., Ligorini A., Ullio P., Grasso D., 2017, *Journal of Cosmology and Astroparticle Physics*, 2017, 015–015
- Gardner S., Yanny B., et al., 2021, *Progress in Particle and Nuclear Physics*, 120, 103904
- Geballe T. R., Oka T., 2010, *The Astrophysical Journal Letters*, 709, L70
- Guessoum N., Ramaty R., Lingenfelter R. E., 1991, *The astrophysical Journal*, 378, 170
- Guessoum N., Jean P., Gillard W., 2005, *Astron. Astrophys.*, 436, 171
- Guessoum N., Jean P., Prantzos N., 2006, *Astronomy & Astrophysics*, 457, 753–762
- Haymes R. C., Walraven G. D., Meegan C. A., Hall R. D., Djuth F. T., Shelton D. H., 1975, *The Astrophysical Journal*, 201, 593
- Hooper D., Blasi P., Serpico P. D., 2009, *Journal of Cosmology and Astroparticle Physics*, 2009, 025–025
- III W. N. J., Jr. F. R. H., Haymes R. C., 1972, *The Astrophysical Journal Letters*, 172, L1
- Indriolo N., Fields B. D., McCall B. J., 2009, *The Astrophysical Journal*, 694, 257
- Indriolo N., et al., 2015, *The Astrophysical Journal*, 800, 40
- Jean, P. et al., 2009, *A&A*, 508, 1099
- Jean P., Knödseder J., Gillard W., Guessoum N., Ferrière K., Marcowith A., Lonjou V., Roques J. P., 2005, *Astronomy & Astrophysics*, 445, 579–589
- Kantzas D., Calore F., 2024, *Astronomy & Astrophysics*, 690, A87
- Kierans C. A., et al., 2019, Positron Annihilation in the Galaxy (arXiv:1903.05569), <https://arxiv.org/abs/1903.05569>

Knödseder J., Jean P., Lonjou V., Weidenspointner M., et al. 2005, *Astronomy & Astrophysics*, 441, 513

Knödseder J., Sabri K., Jean P., von Ballmoos P., Skinner G., Collmar W., 2025, *Astronomy & Astrophysics*, 700, A257

Korol V., Rossi E. M., Barausse E., 2018, *Monthly Notices of the Royal Astronomical Society*, 483, 5518–5533

Krause J., Morlino G., Gabici S., 2015, CRIME - cosmic ray interactions in molecular environments ([arXiv:1507.05127](https://arxiv.org/abs/1507.05127)), <https://arxiv.org/abs/1507.05127>

Landstreet J. D., 2002, Beta and Gamma Decays: Lecture 11, Physics 467/519b Notes, Online lecture notes, Department of Physics & Astronomy, University of Western Ontario, https://physics.uwo.ca/~jlandstr/p467/lec11-beta_gamma/

Launhardt R., Zylka R., Mezger P. G., 2002, *Astronomy & Astrophysics*, 384, 112–139

Le Petit F., Ruard M., Bron E., Godard B., Roueff E., Languignon D., Le Bourlot J., 2016, *Astronomy & Astrophysics*, 585, A105

Leventhal M., MacCallum C. J., Stang P. D., 1978, *The Astrophysical Journal*, 225, L11

Li H., Liang E. P., 1996, *Astrophysical Journal*, 458, 514

Licquia T. C., Newman J. A., 2015, *The Astrophysical Journal*, 806, 96

Limpert E., Stahel W. A., Abbt M., 2001, *BioScience*, 51, 341

Minniti D., et al., 2010, *New Astronomy*, 15, 433

Mirabel I. F., Rodríguez L. F., Cordier B., Paul J., Lebrun F., 1992, *Nature*, 358, 215

Murgia S., 2020, *Annual Review of Nuclear and Particle Science*, 70, 455

Muru M. M., Silk J., Libeskind N. I., Gottl"ober S., Hoffman Y., 2025, *Physical Review Letters*, 135, 161005

Nataf D. M., et al., 2013, *ApJ*, 769, 88

Navarro J. F., Frenk C. S., White S. D., 1996, *Astrophys. J.*, 462, 563

Navarro J. F., et al., 2004, *Mon. Not. Roy. Astron. Soc.*, 349, 1039

Nie J., Lopez-Corredoira M., Liu C., Wang H.-F., Simion I., 2026, *Research in Astronomy and Astrophysics*

Obolentseva M., et al., 2024, *The Astrophysical Journal*, 973, 142

Oka T., Geballe T. R., 2020, *The Astrophysical Journal*, 902, 9

Oka T., Geballe T. R., Goto M., Usuda T., McCall B. J., 2005, *The Astrophysical Journal*, 632, 882–893

Padovani M., Galli D., Glassgold A. E., 2009, *Astronomy & Astrophysics*, 501, 619–631

Paredes J. M., 2005, *Chinese Journal of Astronomy and Astrophysics*, 5, 121

Phan V. H. M., Morlino G., Gabici S., 2018, *Monthly Notices of the Royal Astronomical Society*

Phan V. H. M., Recchia S., Mertsch P., Gabici S., 2023, *Physical Review D*, 107

Portail M., Wegg C., Gerhard O., 2015, *Monthly Notices of the Royal Astronomical Society*, 450, L66

Prantzos N., et al., 2011, *Reviews of Modern Physics*, 83, 1001–1056

Ravikularaman S., Recchia S., Phan V. H. M., Gabici S., 2025, *Astronomy & Astrophysics*, 694, A114

Siegert T., 2023, *Astrophysics and Space Science*, 368, 27

Siegert T., Diehl R., Khachatryan G., Krause M. G. H., Guglielmetti F., Greiner J., Strong A. W., Zhang X., 2016b, *Astronomy & Astrophysics*, 586, A84

Siegert T., Diehl R., Khachatryan G., Krause M. G. H., Guglielmetti F., Greiner J., Strong A. W., Zhang X., 2016a, *Astronomy & Astrophysics*, 586, A84

Siegert T., Crocker R. M., Macias O., Panther F. H., Calore F., Song D., Horiuchi S., 2022, *Monthly Notices of the Royal Astronomical Society: Letters*, 509, L11

Sizun P., Cassé M., Schanne S., 2006, *Physical Review D*, 74, 063514

Skinner G., Diehl R., Zhang X. L., Bouchet L., Jean P., 2015, in Proceedings of the 10th INTEGRAL Workshop: A Synergistic View of the High-Energy Sky. p. 054, doi:10.22323/1.228.0054, <https://pos.sissa.it/228/054/>

Smith D. M., Leventhal M., Cavallo R., et al., 1996, *Astrophysical Journal*, 458, 576

Stabin M., Siegel J. A., 1979, *Medical Physics*, 6, 523

Stecker F. W., 1969, *apss*, 3, 579

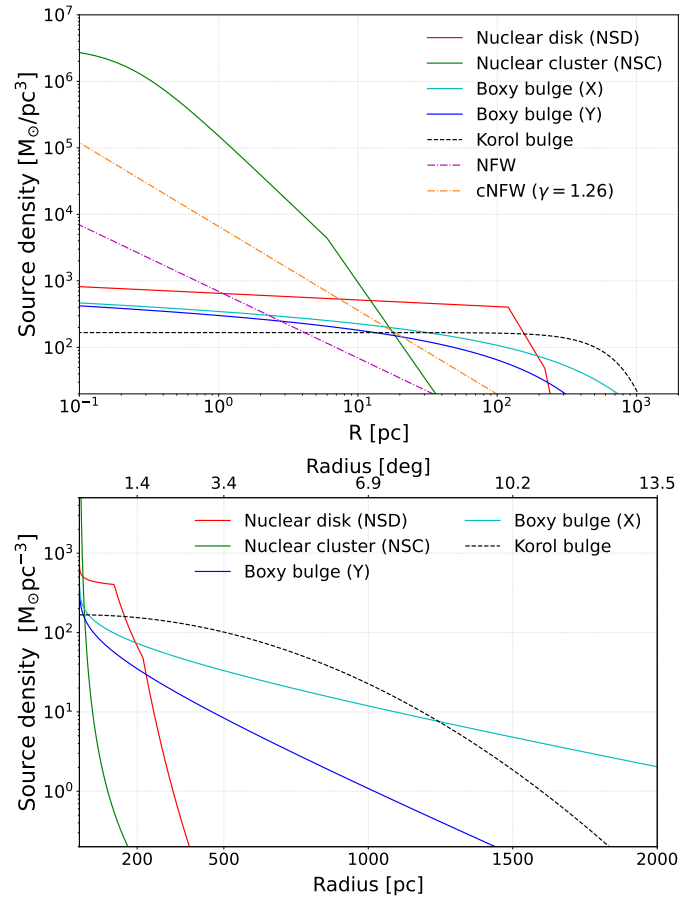


Figure A1. Same as shown in Fig. 1, but including the dark matter density distribution expected from a Navarro-Frenk-White with inner slopes of 1 (classical NFW) and 1.26 (referred to as cNFW in the legend). The left panel focuses on the inner Galaxy, using a logarithmic x-axis, while the right panel uses a linear scale to highlight the large-scale behavior.

Timokhin A. N., 2010, *MNRAS*, 408, 2092

Totani T., 2006, *Publications of the Astronomical Society of Japan*, 58, 965

Weidenspointner G., et al., 2006, *Astronomy & Astrophysics*, 450, 1013

Yüksel H., Kistler M. D., Stanev T., 2009, *Physical Review Letters*, 103

la Torre Luque; Pedro D., Balaji S., Fairbairn M., Sala F., Silk J., 2025, *JCAP*, 09, 034

van der Tak F. F. S., Belloche A., Schilke P., Güsten R., Philipp S., Comito C., Bergman P., Nyman L.-A., 2006, *Astronomy & Astrophysics*, 454, L99–L102

APPENDIX A: EXTRA MATERIAL

In Fig. A1 we show a comparison of the different models for the distribution of sources at the bulge with the dark matter density distribution expected from a Navarro-Frenk-White parametrization and the same but with an inner slope (often also called contraction index) of 1.26 (similar to the one associated to the GCE). Both panels show the source density as a function of radial distance for each model, as in Fig. 1.

For completeness we also show the injection spectra used for the different parametrizations adopted in this work, and with the normalizations used (found from imposing a total positron injection rate that matches the 511 keV observations), in Fig. A2.

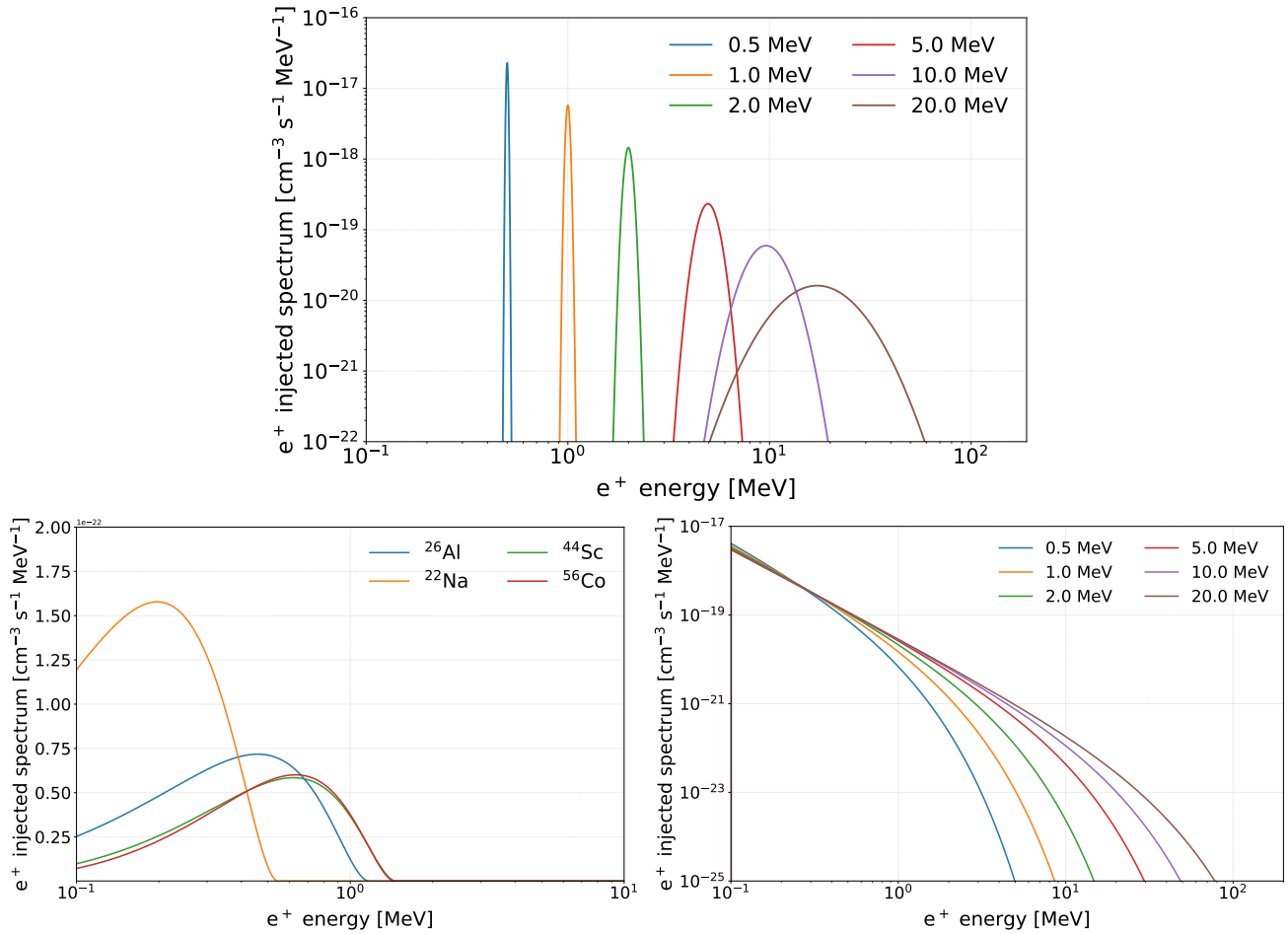


Figure A2. Positron injection spectra for the parametrizations used in this work. Here, we show the spectra normalized to a total positron injection rate of $2 \cdot 10^{43} \text{ e}^+/\text{s}$, adopting a distribution of sources following the spatial distribution of a combination of the nuclear stellar disk, nuclear stellar cluster and the boxy-bulge distributions. The top panel refers to the case of assuming log-normal injection spectra, the left panel to the case of radionuclides injecting the positrons and the right panel to a power-law positron injection. In the top panel, the different colors refer to different E_{mean} values, all for $f=1/50$. In the left panel, the different colors indicate the ionization rate from the radionuclides discussed in the main text. In the right panel, the different colors indicate different cut-off energies. In this panel, solid lines correspond to a power-law where the spectral index is $\gamma = 2.2$, while the dashed lines correspond to a power-law of $\gamma = 1.2$.

Additionally, we show in the left panel of Fig. A3 the positron spectrum after energy losses for the general logarithmic injection described above. In the right panel of that figure, we show the ionization cross sections employed in this work, compared with those from charge-exchange with molecular hydrogen. Interestingly, both of them peak at a similar value of $\sim 10^{-16} \text{ cm}^{-2}$. However, the charge-exchange cross sections are concentrated between 10-100 eV, whereas the ionization cross sections are still significant up to higher energies. Including the ionization produced from the charge-exchange process can be challenging, since it would mainly depend on the gas temperature (below the eV for a cold gas like that of the CMZ) and other details on how the positrons become thermal. If positrons thermalize below 10 eV, what can be expected for the cold gas in the CMZ, the charge-exchange process would lead to a negligible ionization in this region.

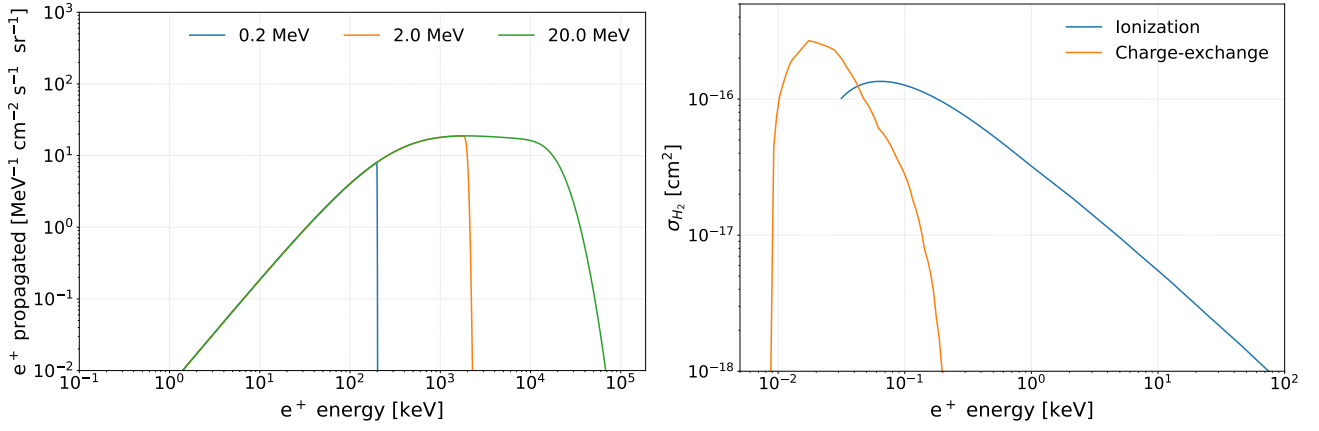


Figure A3. Left panel: Positron spectrum after energy losses for the general log-normal injection described above. The colors represent different mean injection energies of the log-normal distribution, as indicated in the legend. The spectra overlap at low energies because they depend on the energy integral (Eq. 9), which is normalized to be the same for all signals (Eq. 10). **Right panel:** A comparison of the ionization cross sections of molecular hydrogen, with those of charge-exchange, which could potentially contribute to the CMZ ionization too.